Supplementary material

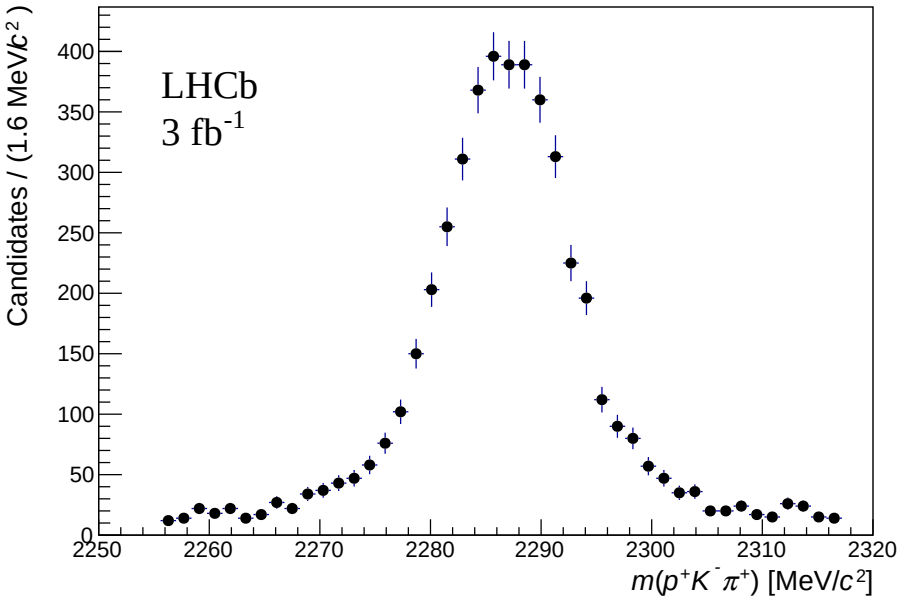

Figure 1: Distribution of the $pK^-\pi^+$ invariant mass for all $\Lambda_b^0 \to \Lambda_c^+ \tau^- \overline{\nu}_\tau$ candidates in the final fit sample.

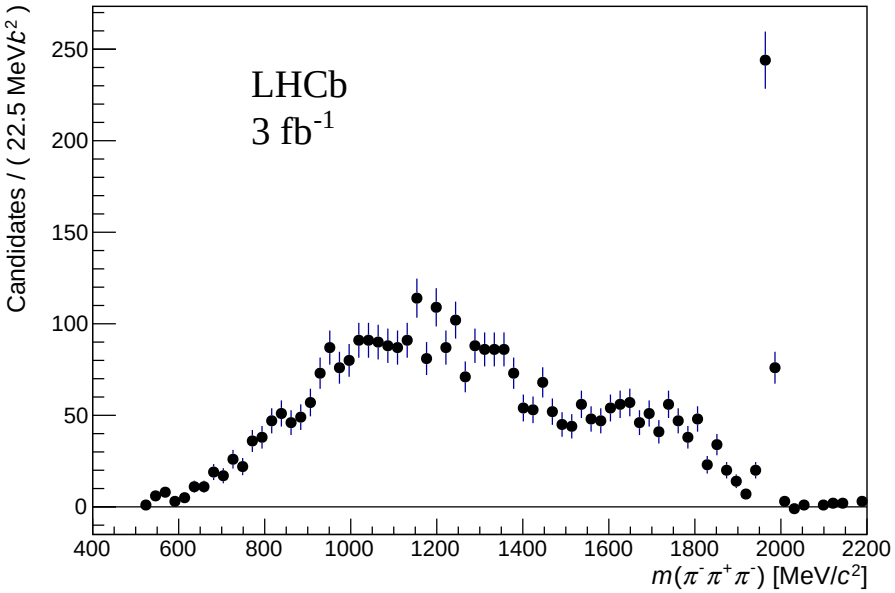

Figure 2: Distribution of the $\pi^-\pi^+\pi^-$ invariant mass for all $\Lambda_b^0 \to \Lambda_c^+\tau^-\overline{\nu}_\tau$ candidates after the Λ_c^+ sideband subtraction passing the inverted topology requirement.

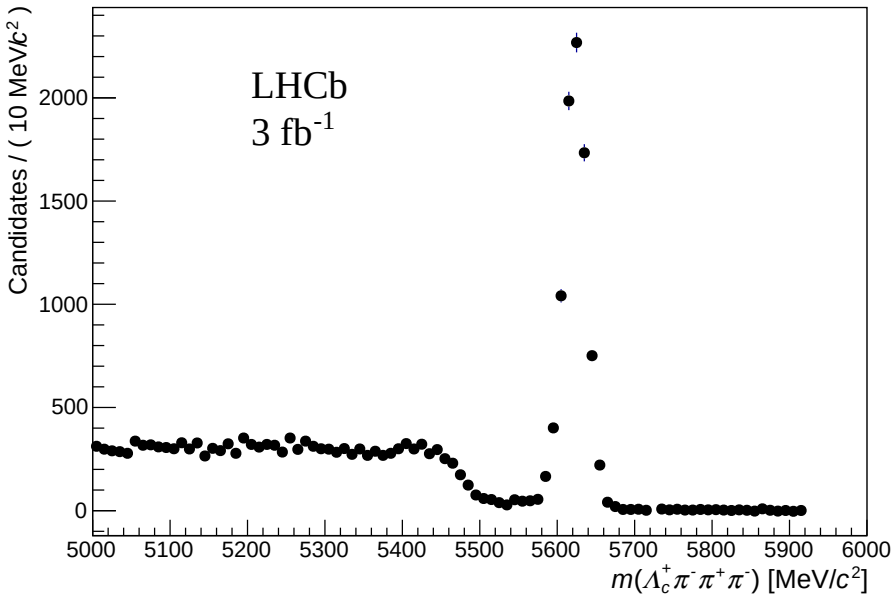

Figure 3: Distribution of the $\Lambda_c^+\pi^-\pi^+\pi^+$ invariant mass for all $\Lambda_b^0 \to \Lambda_c^+\tau^-\overline{\nu}_\tau$ candidates after the Λ_c^+ sideband subtraction.

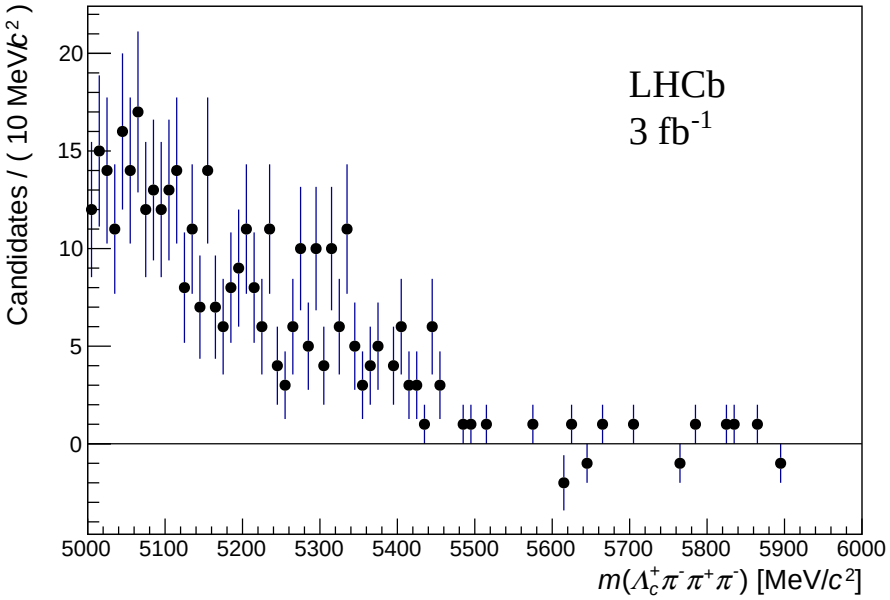

Figure 4: Distribution of the $\Lambda_c^+\pi^-\pi^+\pi^+$ invariant mass for all $\Lambda_b^0 \to \Lambda_c^+\tau^-\overline{\nu}_\tau$ candidates after the Λ_c^+ sideband subtraction passing the inverted vertex topology requirement.

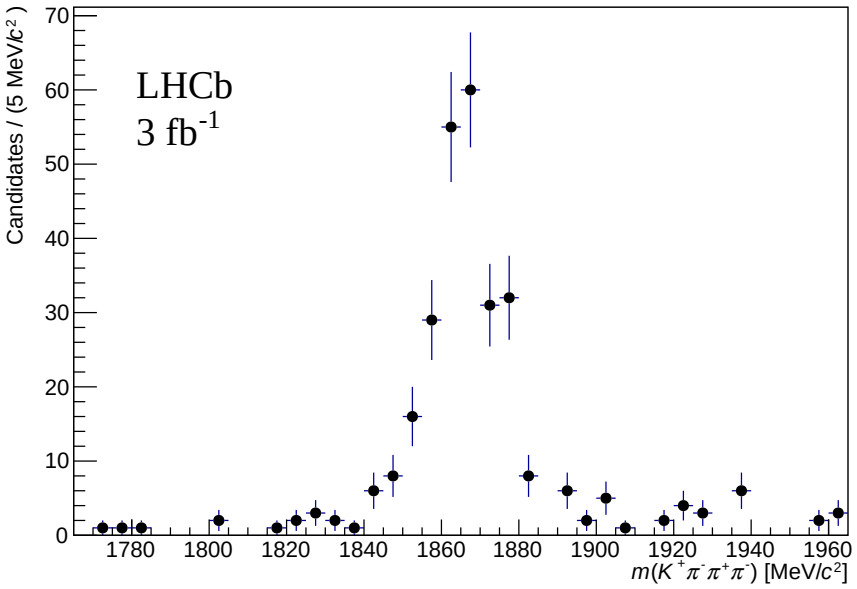

Figure 5: Distribution of the $K^+\pi^-\pi^+\pi^-$ invariant mass for all $\Lambda_b^0 \to \Lambda_c^+ \overline{D}^0\, X$ candidates where a kaon track is found compatible with the 3π vertex.

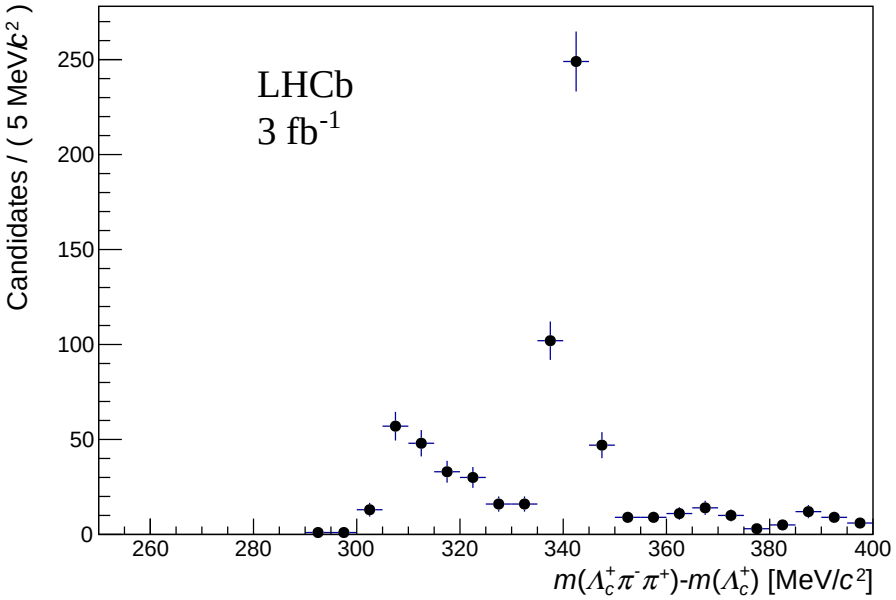

Figure 6: Distribution of the difference between $\Lambda_c^+\pi^-\pi^+$ invariant mass and the Λ_c^+ invariant mass for all candidates reconstructed in the $\Lambda_b^0 \to \Lambda_c^+\pi^-\pi^+\pi^-$ normalisation channel peak.

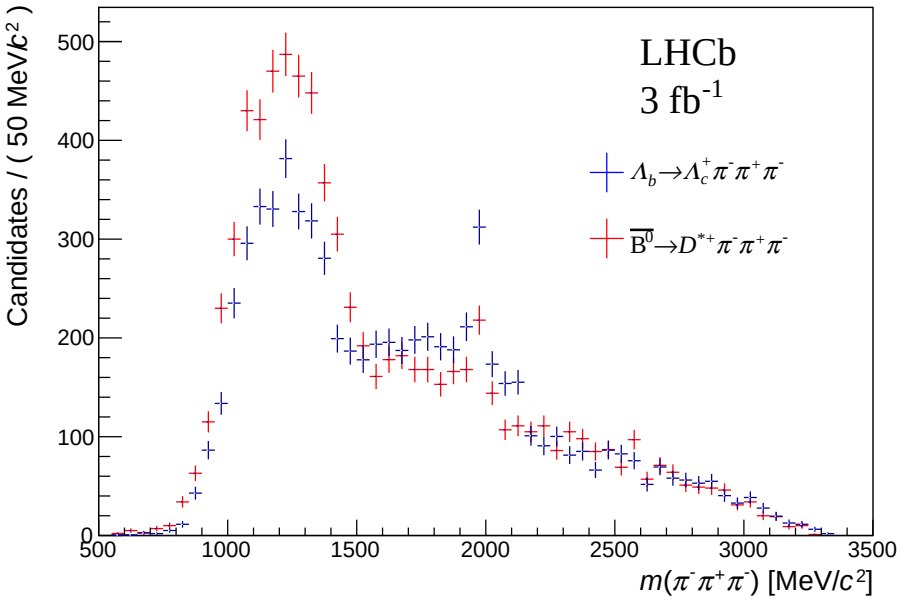

Figure 7: Distribution of the $\pi^-\pi^+\pi^-$ invariant mass for all candidates in (blue) the $\Lambda_b^0 \to \Lambda_c^+\pi^-\pi^+\pi^-$ channel where the Λ_c^{*+} contributions have not been removed and in (red) the $\overline{B}^0 \to D^{*+}\pi^-\pi^+\pi^-$ channel. The two distributions are normalised to the same area.

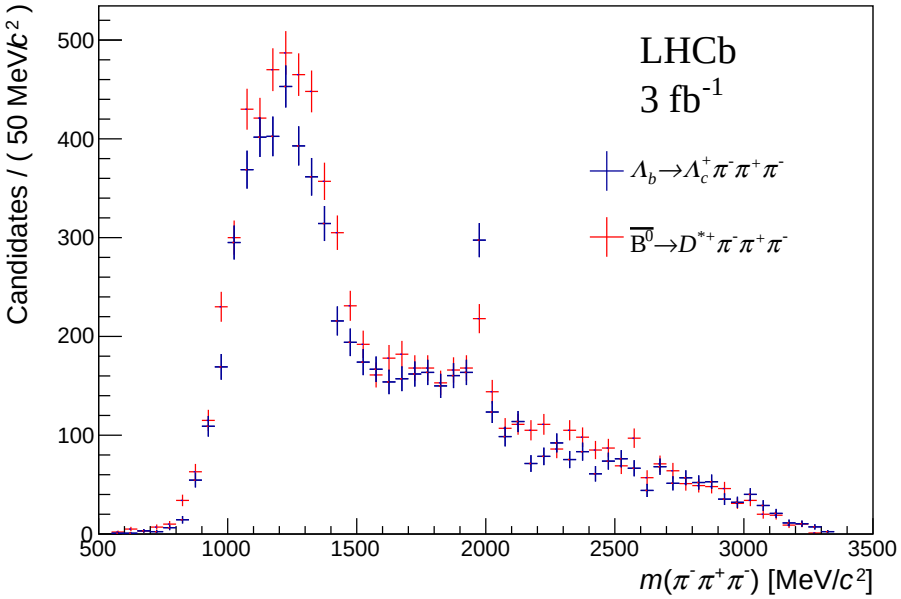

Figure 8: Distribution of the $\pi^-\pi^+\pi^-$ invariant mass for all candidates in (blue) the $\Lambda_b^0 \to \Lambda_c^+\pi^-\pi^+\pi^-$ channel where the Λ_c^{*+} contributions have been removed and in (red) the $\overline{B}^0 \to D^{*+}\pi^-\pi^+\pi^-$ channel. The two distributions are normalised to the same area.

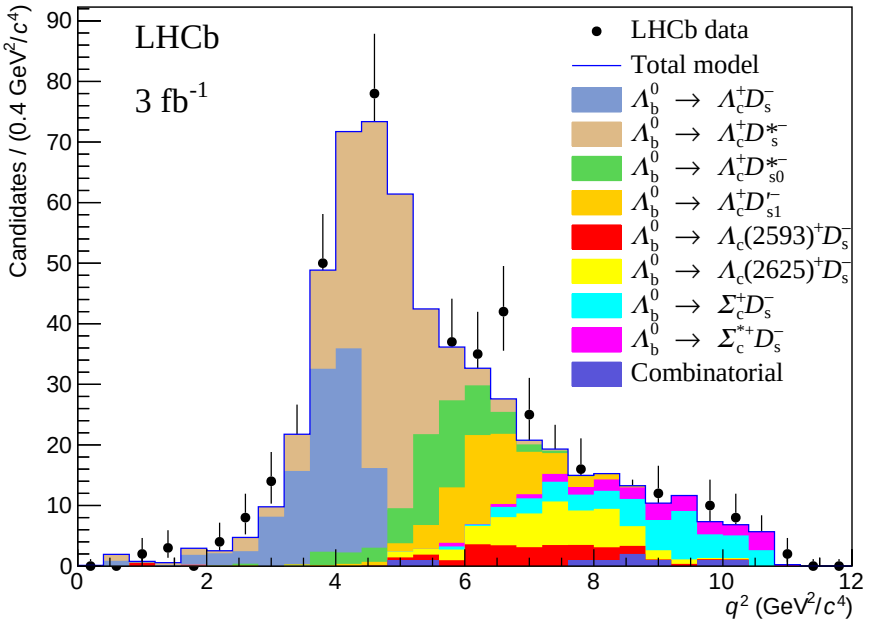

Figure 9: Distribution of q^2 for all candidates in the $\Lambda_c^+ 3\pi$ control sample where the mass of the 3π system is selected around the D_s^- mass. The rates of the various components indicated in the legend are taken for the fit results to the $\Lambda_c^+ 3\pi$ mass fit described in the paper.

Parameter	Fit result	Constraint value
N_{sig}	349 ± 40 (11.8%)	
$f_{\tau\to 3\pi\nu}$		0.78
$f_{\Lambda_c^*\tau\overline{\nu}_\tau}$		0.1
$N_{D^0}^{same}$	80.2 ± 8.3	81.4 ± 7.4
$f_{D^0}^{v_1-v_2}$	1.3 ± 0.7	
N_{D_s}	2755.9 ± 81	
f_{D_s}	0.49 ± 0.09	0.65 ± 0.08
$f_{D_{s0}^*}$	0.0 ± 0.012	0.28 ± 0.12
$f_{D_{s1}'}$	0.41 ± 0.07	0.29 ± 0.12
$f_{\Lambda_c(2625)D_s^{(*)}}$	0.19 ± 0.06	0.22 ± 0.09
$f_{\Sigma_c\pi D_s^{(*)}}$	0.0 ± 0.02	0.22 ± 0.05
N_{D^+}	443 ± 54	
N_{combi}		40.3
$N_{\Lambda_c^+}^{bkg}$		639
χ^2	256	
reduced χ^2 ($ndof = 216$)	1.30	

Table 1: Nominal fit results. The parameter $f_{\tau\to 3\pi\nu}$ is the relative abundance of the $\tau^- \to 3\pi\nu$ candidates wrt to all τ^- candidates; $f_{\Lambda_c^*\tau\overline{\nu}_\tau}$ is the relative yield of $\Lambda_b^0 \to \Lambda_c^{*+}\tau^-\overline{\nu}_\tau$ candidates wrt to the signal yield; $N_{D^0}^{same}$ is the number of $\Lambda_b^0 \to \Lambda_c^+\overline{D}^0 X$ candidates where the 3 pions originate from the same vertex; $f_{D^0}^{v_1-v_2}$ is the relative yield of $\Lambda_b^0 \to \Lambda_c^+\overline{D}^0 X$ candidates where the 3 pions do not originate from the same vertex wrt to the simulation prediction; N_{D_s} is the total number of $\Lambda_b^0 \to \Lambda_c^+ D_s^-(X)$ candidates; f_{D_s}, $f_{D_{s0}^*}$, $f_{D_{s1}'}$, $f_{\Lambda_c(2625)D_s^{(*)}}$, $f_{\Sigma_c\pi D_s^{(*)}}$ are the relative yields of $\Lambda_b^0 \to \Lambda_c^+ D_s^-$, $\Lambda_b^0 \to \Lambda_c^+ D_{s0}^*$, $\Lambda_b^0 \to \Lambda_c^+ D_{s1}'$, $\Lambda_b^0 \to \Lambda_c(2625)D_s^{(*)}$, $\Lambda_b^0 \to \Sigma_c\pi D_s^{(*)}$ decays wrt to that of the $\Lambda_b^0 \to \Lambda_c^+ D_s^{*-}$ channel, respectively; N_{D^+} is the yield of $\Lambda_b^0 \to \Lambda_c^+ D^-(X)$ candidates; N_{combi}, $N_{\Lambda_c^+}^{bkg}$ are the yields of combinatorial and misreconstructed Λ_c^+ background, respectively.

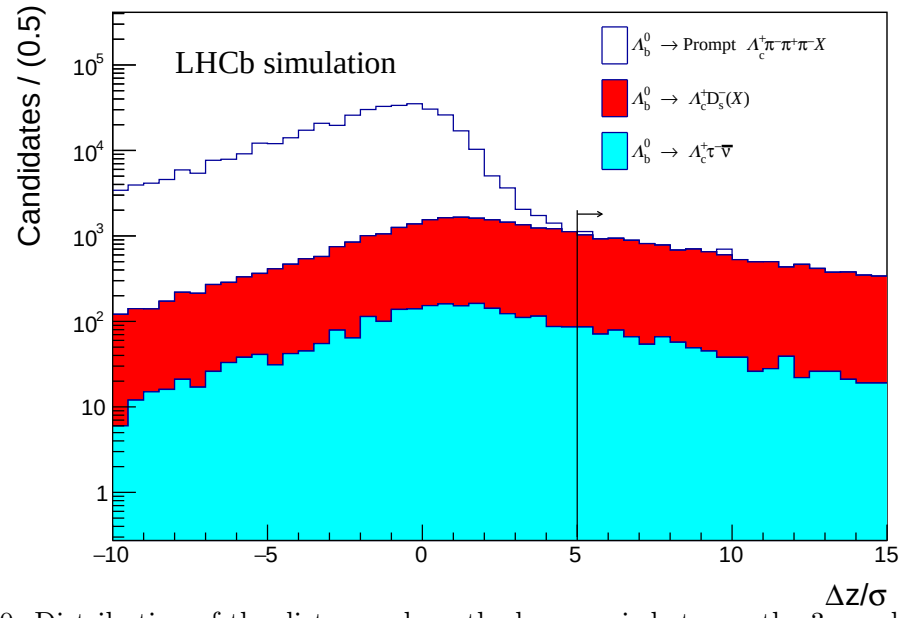

Figure 10: Distribution of the distance along the beam axis between the 3π and the Λ_c^+ vertices, divided by its error, for signal, $\Lambda_b^0 \to \Lambda_c^+ D_s^-(X)$ and prompt candidates, as indicated in the legend. The vertical line represents the required inverted topology requirement of 5σ.

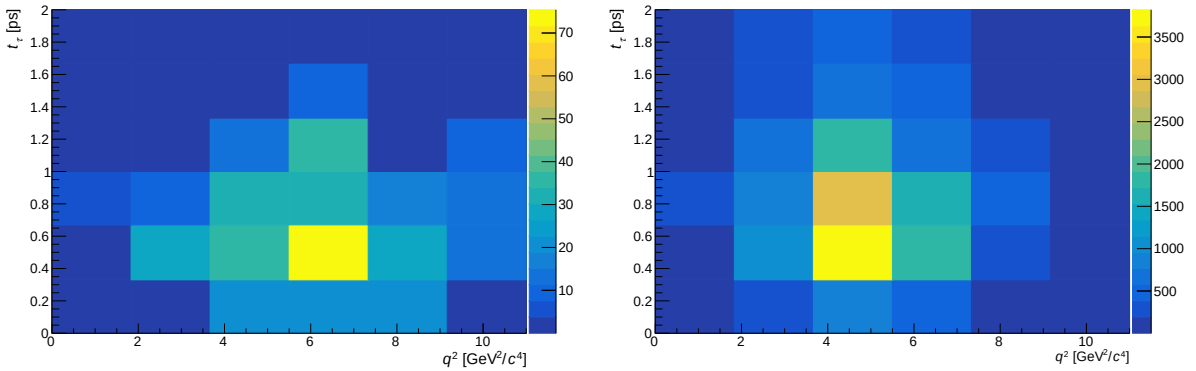

Figure 11: Distribution of t_τ versus q^2 variables for BDT output<0.66 in the simulation, for (left) $\Lambda_b^0 \to \Lambda_c^+\tau^-\overline{\nu}_\tau$ candidates and (right) $\Lambda_b^0 \to \Lambda_c^+ D_s^-(X)$ candidates.

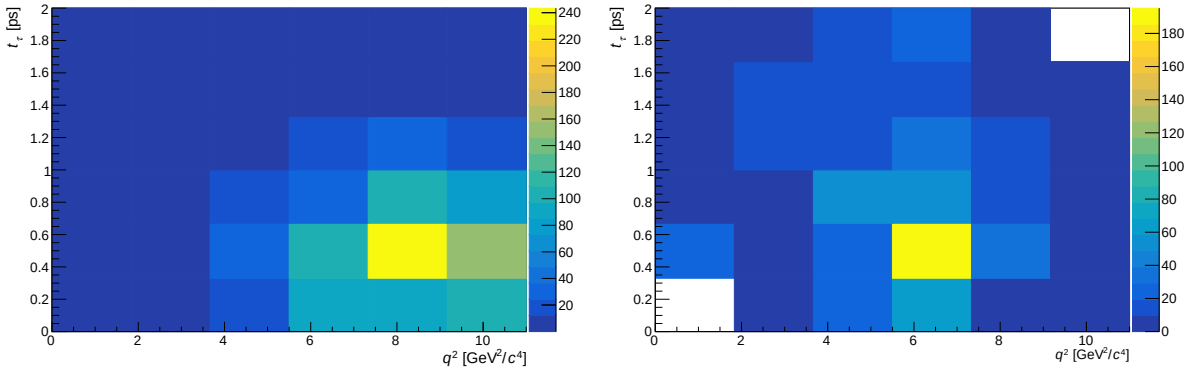

Figure 12: Distribution of t_τ versus q^2 variables for BDT output>0.66 in the simulation, for (left) $\Lambda_b^0 \to \Lambda_c^+ \tau^- \overline{\nu}_\tau$ candidates and (right) $\Lambda_b^0 \to \Lambda_c^+ D_s^-(X)$ candidates.

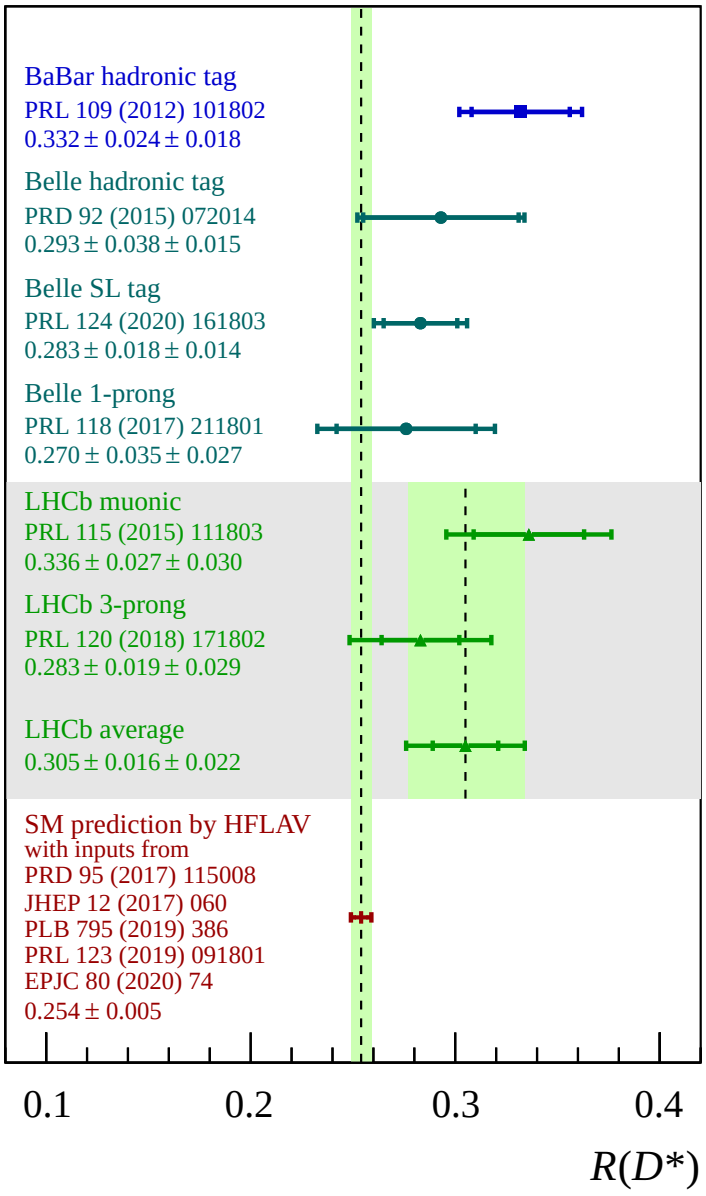
BaBar hadronic tag
PRL 109 (2012) 101802
0.332 ± 0.024 ± 0.018
Belle hadronic tag
PRD 92 (2015) 072014
0.293 ± 0.038 ± 0.015
Belle SL tag
PRL 124 (2020) 161803
0.283 ± 0.018 ± 0.014
Belle 1-prong
PRL 118 (2017) 211801
0.270 ± 0.035 ± 0.027
LHCb muonic
PRL 115 (2015) 111803
0.336 ± 0.027 ± 0.030
LHCb 3-prong
PRL 120 (2018) 171802
0.283 ± 0.019 ± 0.029
LHCb average
0.305 ± 0.016 ± 0.022
SM prediction by HFLAV
with inputs from
PRD 95 (2017) 115008
JHEP 12 (2017) 060
PLB 795 (2019) 386
PRL 123 (2019) 091801
EPJC 80 (2020) 74
0.254 ± 0.005
0.1
0.2
0.3
0.4
R(D*)

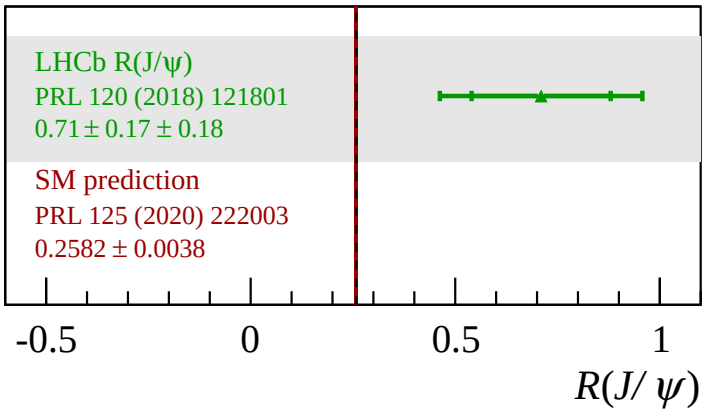
LHCb R(J/ψ)
PRL 120 (2018) 121801
0.71 ± 0.17 ± 0.18
SM prediction
PRL 125 (2020) 222003
0.2582 ± 0.0038
-0.5
0
0.5
1
R(J/ψ)

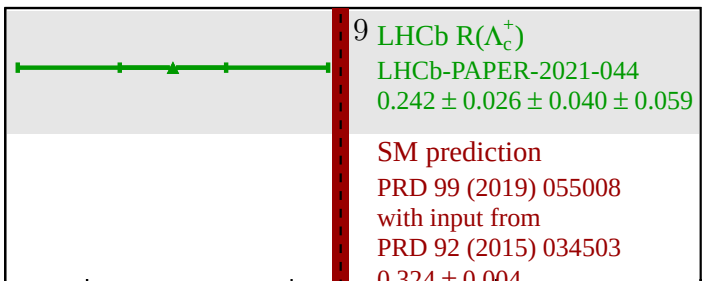
LHCb R(Λc+)
LHCb-PAPER-2021-044
0.242 ± 0.026 ± 0.040 ± 0.059
SM prediction
PRD 99 (2019) 055008
with input from
PRD 92 (2015) 034503
0.324 ± 0.004